

Effects of Strain-Induced Pseudogauge Fields on Exciton Dispersion, Transport, and Interactions in Transition Metal Dichalcogenides

Shiva Heidari,¹ Shervin Parsi,^{1,2} and Pouyan Ghaemi^{1,2}

¹*Physics Department, City College of the City University of New York, NY 10031, U.S.A.*

²*Physics Program, Graduate Center of City University of New York, NY 10031, U.S.A.*

We study the effects of strain on exciton dynamics in transition metal dichalcogenides (TMDs). Using the Bethe-Salpeter formalism, we derive the exciton dispersion relation in strained TMDs and demonstrate that strain-induced pseudo-gauge fields significantly influence exciton transport and interactions. Our results show that low-energy excitons occur at finite center-of-mass momentum, leading to modified diffusion properties. Furthermore, the exciton dipole moment depends on center-of-mass momentum, which enhances exciton-exciton interactions. These findings highlight the potential of strain engineering as a powerful tool for controlling exciton transport and interactions in TMD-based optoelectronic and quantum devices.

I. INTRODUCTION

The realization of excitons with large binding energies in two-dimensional transition metal dichalcogenides (TMDs) presents new opportunities for studying and utilizing exciton transport, even at room temperature [1–6]. A key challenge in this context is controlling exciton motion in a specific direction and over large distances, particularly at room temperature.

Another advantage of two-dimensional materials is their ability to be strained in a controlled manner. The effects of strain on excitonic states and their diffusion have been studied both theoretically and experimentally [3, 7–10]. Most previous studies have explored the influence of strain on excitons in terms of local potentials—that is, the shift in electronic energy bands [7, 11, 12]. Strain also induces symmetry breaking and fine-structure modifications in excitons, as observed in recent studies [13]. Another notable effect of strain in two-dimensional materials, extensively studied in graphene, is the generation of a pseudomagnetic field that leads to the formation of flat Landau levels [14–16]. This effect in graphene can give rise to phenomena such as the fractional quantum Hall effect [17, 18] and Landau-level excitons [19]. Despite their gapped band structure, TMDs can exhibit similar effects, where the conduction and valence bands transform into a set of Landau-like bands [20–22]. Similar to graphene, this strain-induced effect in TMDs can be described in terms of pseudo-gauge fields. The strain-induced bands are separated by a finite gap, which is controlled by the magnitude of the applied strain. A few percent of lattice deformation can induce a gap on the order of room temperature [23].

In this paper, we examine the effect of strain-induced modifications in the electronic band structure, resulting from pseudo-gauge fields, on excitonic transport in TMDs. Our results indicate that such modifications in the electronic band structure lead to enhanced anisotropic exciton diffusion, well beyond the effects of strain-induced local potentials. Another key property of electronic bands in TMDs is the presence of band inversion near the bottom of the bands in each valley [24–26].

Although the presence of an even number of valleys renders the full band structure topologically trivial, the possibility of optically selective coupling with the bands in each valley leads to observable effects of nontrivial band topology within an individual valley [27]. We show that in the presence of band inversion, strain shifts the exciton energy band minimum to a finite momentum and stabilizes dark excitons, which naturally have a longer lifetime [28]. These effects collectively support extensive unidirectional exciton diffusion.

Beyond its influence on exciton transport, strain can also enhance exciton-exciton interactions. Under the type of strain discussed in this paper, the electronic states resemble the Hall electronic states in the Landau gauge [29]. These states are labeled by their momentum along the nanoribbon, and the maximum of their spatial wavefunction distribution in the perpendicular direction is controlled by the parallel momentum. As a result, excitons with finite center-of-mass momentum are formed by binding electrons and holes that are spatially separated in a plane. This structure, which leads to a large in-plane dipole moment, facilitates strong exciton-exciton interactions [30]. Our results show that pseudo-gauge fields generated by specific strain patterns provide an efficient avenue for simultaneously facilitating exciton transport and strong exciton-exciton interactions. Consequently, strain engineering emerges as a powerful tool for realizing and utilizing novel excitonic phases in TMDs, through effects that go beyond the mere generation of local potentials.

The remainder of this paper is organized as follows. In Section II, we describe the exciton band structure in strained TMDs using the Bethe-Salpeter formalism. Section III presents our results on exciton diffusion in strained TMDs, where we analyze the effects of strain-induced pseudo-gauge fields on exciton transport and demonstrate how strain enhances directional diffusion. Section IV discusses the implications of strain on exciton mobility, including its temperature dependence and its role in enabling efficient excitonic transport. Finally, in Section V, we summarize our key findings and discuss potential applications of strain-engineered TMDs in excitonic devices and quantum information technologies.

II. EXCITONIC DISPERSION IN STRAINED TMDS

Excitonic states arise from the attractive Coulomb interaction between electrons in the conduction band and holes in the valence band [31–34]. The effective Hamiltonian H_0 for the electrons close to the center of each valley in strained monolayer MoS₂, which is derived using Slater-Koster tight-binding method [20, 35], reads as:

$$H_0 = \begin{pmatrix} \mathcal{V}_+(y) - \frac{\hbar^2}{4m_0}(\alpha + \beta)\partial^2 y & t_0 a_0(q_x + \frac{e}{\hbar}A_{1,x}) - t_0 a_0 \partial_y \\ t_0 a_0(q_x + \frac{e}{\hbar}A_{1,x}) - t_0 a_0 \partial_y & \mathcal{V}_-(y) - \frac{\hbar^2}{4m_0}(\alpha - \beta)\partial^2 y \end{pmatrix}. \quad (1)$$

The parameters in H_0 are $t_0 = 2.34$ eV, $\alpha = -0.01$ and $\beta = -1.54$. \hbar and e are the Planck reduced constant and elementary charge, respectively and a_0 is the MoS₂ lattice parameter. The potential terms $\mathcal{V}_\pm(y)$ in H_0 which incorporates spin-orbit interaction is given by [20]

$$\mathcal{V}_\pm(y) = \frac{(\Delta_0 + \lambda_0) \pm (\Delta + \lambda)}{2} + \mathcal{D}_\pm(y) + \delta\lambda_\pm(y) + \frac{\hbar^2}{4m_0}\alpha(q_x + \frac{e}{\hbar}A_{2,x})^2 + \frac{\hbar^2}{4m_0}\alpha(q_x + \frac{e}{\hbar}A_{3,x})^2. \quad (2)$$

The potential $\mathcal{V}_\pm(y)$ includes spin-dependent energy gaps $(\Delta_0, \Delta) = (-0.11, 1.82)$ eV and spin-orbit parameters $(\lambda_0, \lambda) = (69, 1.82)$ meV. The Spatially varying terms $\mathcal{D}_\pm(y)$ and $\delta\lambda_\pm(y)$ are given by [20],

$$D_\pm(y) = \alpha_1^\pm |\mathcal{A}|^2 + \alpha_2^\pm (\hat{V} + \omega_{xy}^2) + \alpha_3^\pm \hat{V}^2, \quad (3)$$

$$\delta\lambda_\pm(y) = \alpha_1^{s\pm} |\mathcal{A}|^2 + \alpha_2^{s\pm} (\hat{V} + \omega_{xy}^2) + \alpha_3^{s\pm} \hat{V}^2.$$

The parameters in Eq. 3 are given in table II. The Hamiltonian in Eqn. (1) incorporates the effect of strain on the electronic structure through the strain parameter \mathcal{A} and the corresponding gauge field \mathbf{A}_i as follows: The strain leads to a deformation in the positions of the lattice sites from the original position \mathbf{r}_0 to $\mathbf{r}_0 + \mathbf{r}_0 \cdot \nabla \mathbf{u}$ [36]. An arc-shaped deformation is imposed on the nanoribbon, characterized by the displacement profile $(u_x, u_y) = (xy/R, -x^2/2R)$, where R denotes the radius of curvature. In the effective low-energy Hamiltonian in Eq.(1) the lattice deformation generates an effective gauge field A_i given by $\mathbf{A}_i = \eta_i (\hbar/ea_0) (\text{Re}[\mathcal{A}], \text{Im}[\mathcal{A}])$. Here, the variables η_i are effective couplings that are determined based on the parameters of the tight-binding model [20]. The strain-dependent parameters are defined as: $\mathcal{A} = \varepsilon_{xx} - \varepsilon_{yy} - i2\varepsilon_{xy}$, $\hat{V} = \varepsilon_{xx} + \varepsilon_{yy}$, and $\omega_{xy} = (\partial u_y / \partial x - \partial u_x / \partial y) / 2$, where $\varepsilon_{ij} = \frac{1}{2} (\partial u_i / \partial r_j + \partial u_j / \partial r_i)$ is the strain tensor components in the plane. The term \hat{V} represents the local potential generated by strain, whose effects on excitonic transport have been previously studied [7, 10]. The effective vector potential resulting from the strain pattern described above is $\mathbf{A}_i = \frac{\eta_i \hbar}{ea_0} (y/R, 0)$. We focus on the effect of the

emerging gauge field \mathbf{A}_i on excitonic transport, on excitonic transport rather than on the widely studied effect of the strain-induced potential \hat{V} .

	eV		eV		meV		meV
α_1^+	15.99	α_1^-	15.92	α_1^{s+}	-61	α_1^{s-}	-5.7
α_2^+	-3.07	α_2^-	-1.36	α_2^{s+}	3.2	α_2^{s-}	0.02
α_3^+	-0.17	α_3^-	0.0	α_3^{s+}	3.4	α_3^{s-}	0.01

TABLE I. Parameters for strain-induced potential terms in Eq. 3 [20].

The topological character of the Hamiltonian H_0 is determined by the Chern number, expressed as $2\mathcal{C} = \text{sign}(\Delta) - \text{sign}(\beta)$ [27]. The non-zero Chern number, which is connected with a band inversion, mainly affects the orbital character of the bands rather than general shape of the band structure. In the presence of the strain, the effect of the band inversion (i.e. non-zero Chern number) is more apparent and affects the shape of the band structure by pushing the band minimum away from the corner of the Brillouin zone. To derive the band structure of the electronic states in the strained nanoribbon with respect to the momentum along the nanoribbon, we employ trigonal basis functions $T_n(y) = T(y - y_n) = L_y - |y - y_n|(N + 1)$, where $y_n = L_y(\frac{n}{N+1} - \frac{1}{2})$ and $L_y = a_0(N + 1)$ is the width of the nanoribbon [20] [Fig. 2]. The function $T_n(y)$ incorporates the hard boundary condition corresponding to the finite width of the ribbon. The wave function for an arc-shaped monolayer TMD is expanded using a set of $T_n(y)$ as

$$\Psi_k^{c,v}(y) = \begin{pmatrix} \sum_n a_{n,k}^{c,v} T_n(y) \\ \sum_n b_{n,k}^{c,v} T_n(y) \end{pmatrix}, \quad (4)$$

where v, c refer to the valence and conduction bands, respectively. The coefficients $a_{n,k}$ and $b_{n,k}$ represent the spinor components of the wave functions, and n ranges from 0 to N . The orthogonality of the wave function $\Psi_k^{c,v}(y)$ is discussed in the Appendix A. The band structure of the strained TMD is derived by diagonalizing the Hamiltonian in the space of the functions in Eq. (4) which identifies the coefficients $a_{n,k}^{c,v}$ and $b_{n,k}^{c,v}$.

Fig. 1(a) shows the energy dispersion of Hamiltonian (1) corresponding to a nanoribbon with zigzag edges under different arc-shaped strain coupling parameters η_i , where we set $\eta_1 = \eta_2 = \eta_3 = \eta$. As the magnitude of strain increases, the electronic band structure exhibits electron-hole asymmetry and leads to the formation of pseudo-Landau levels [14, 15, 37]. The strain-induced pseudogauge fields A_i lead to the localization of the wave function along the y direction, resulting in modification of the energy bands and increased energy spacing between electronic levels [20]. The comparison of the energy gaps between the first two bands within the original conduction band in unstrained and strained systems is shown in Fig. 1.c. In the unstrained system, a finite-size gap of 116

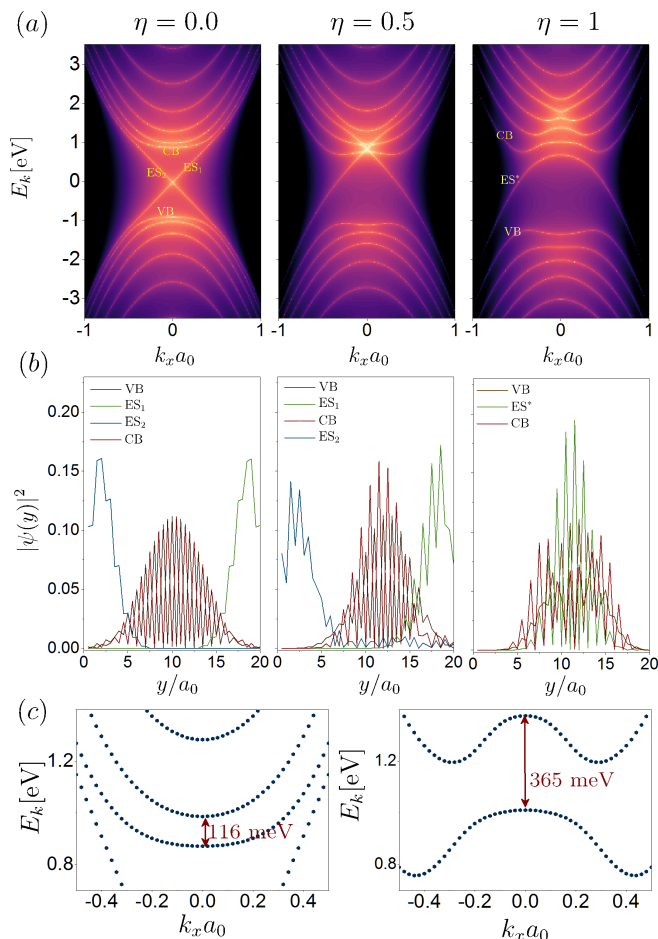


FIG. 1. (a): Quasiparticle energy dispersion of monolayer MoS₂ nanoribbon around $k_x = 0$, for unstrained case, $\eta = 0$, and arc-shaped strained cases, $\eta \neq 0$. We set the width of the nanoribbon to be $L_y = a_0(N + 1)$ with $N = 20$, and arc radius $R = 0.5L_y$. (b): Probability density $|\psi(y)|^2$ of the conduction (CB) and valence (VB) bands and two edge states, plotted against the coordinate $y \in (0, Na_0)$ with $N = 20$ while setting k_x close to zero. At $\eta = 1$, the edge states hybridize and extend fully into the bulk, losing their characteristic edge state signature; these hybridized states are denoted as ES*. (c): Comparison of the energy gaps between the first two conduction bands in unstrained ($\eta = 0$) and strained systems ($\eta = 1$): The finite-size gap in the unstrained system is 116 meV ($T = 1346$ K), while the strain-induced gap in the strained system increases significantly to 365 meV ($T = 4235$ K) for the $\eta = 1$ case.

meV arises due to quantum confinement imposed by the hard boundaries of the ribbon. Compared to room temperature, the finite-size gap may be insufficient to justify the one-dimensional diffusion of excitons [7]. In contrast, the application of strain significantly increases the gap to 365 meV at $\eta = 1$. The strain-induced increase of the gap would support the one-dimensional diffusion of the exciton even at room temperature.

Two-dimensional TMDs demonstrate remarkable mechanical resistance compared to their bulk counterparts.

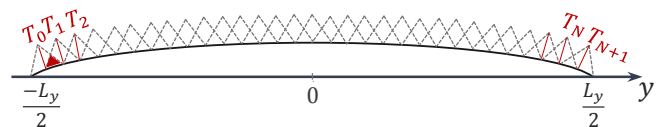


FIG. 2. The trigonal basis function $T_n(y)$ is defined as $T_n(y) = L_y - |y - y_n|(N + 1)$, where $|y| < L_y/2$, and $y_n = L_y \left(\frac{n}{N+1} - \frac{1}{2} \right)$ is the position of the n -th basis function, N is the number of basis functions, and L_y is the width of the nanoribbon along the y -direction. This function is used to satisfy the hard boundary conditions for an arc-shaped monolayer Transition Metal Dichalcogenides (TMDs) system. We note that $\langle T_n | T_{n+1} \rangle \neq 0$.

Although typical bulk semiconductors break down at strains less than 1 %, 2D materials can withstand deformations exceeding 10 % [23, 38, 39]. This extraordinary elasticity allows for significant manipulation of their properties through strain engineering. We characterize the mechanical strain in TMD nanoribbons using the tuning parameter η in our model Hamiltonian. At $\eta = 1$, the strain reaches 6% [Fig. 5(a)], which is within the typical strain tolerance of TMD materials before structural failure occurs. This relationship between the tuning parameter and the percentage of strain allows for precise control and analysis of the mechanical properties of TMD nanoribbons within their elastic regime.

Due to broken translational symmetry along one direction in TMD nanoribbons, the band structure consists of multiple one-dimensional bands, as shown in Fig. 1(a) [40]. Given the topological character of the bands in each individual valley the edge modes are also present. Fig. 1(b) shows the probability density $|\psi(y)|^2$ for the conduction (CB) and valence (VB) bands, along with two edge states (ES₁ and ES₂), corresponding to Fig. 1(a). These are plotted as a function of the coordinate $y \in (0, Na_0)$ along the width, where $N = 20$. In the unstrained nanoribbon ($\eta = 0$), the edge states are well-defined and localized at the edges. As the strain strength increases, these edge states begin to extend into the bulk. For $\eta = 1$, the edge states hybridize and extend fully into the bulk, losing their characteristic edge state signature; we denote these hybridized states as ES*. Strain-induced modifications can extend these edge states into the bulk [14, 15, 41–43]. Given the lack of topological protection due to the opposite parity in the two valleys, we primarily focus on the electronic states in the bulk of the nanoribbon rather than on the edge states in the remainder of the paper.

III. EXCITON BAND STRUCTURE

The electron-hole interaction that leads to the formation of exciton is given by Hamiltonian H_I :

$$H_I = \int V_{(R-R')} \left(\sum_{o,o'=a}^b c_{R,o}^\dagger c_{R',o'}^\dagger c_{R',o'} c_{R,o} \right) d\mathbf{R}d\mathbf{R}'. \quad (5)$$

In the interaction Hamiltonian H_I , $c_{R,o}^\dagger$ ($c_{R,o}$) is the electron creation (annihilation) operator for the spinor o at the position $R = (x, y)$. The interaction potential $V_{(R-R')}$ describes the Coulomb-like interaction between particles at positions R and R' . The reduced Coulomb interaction is described by the Keldysh potential $V(r)$ [44, 45] given by:

$$V(r) = \frac{\pi e^2}{2\epsilon r_0} [\mathcal{H}_0(r/r_0) - Y_0(r/r_0)]. \quad (6)$$

Here, ϵ is the dielectric constant of the substrate on which the 2D material lies. For a MoS₂ monolayer on a SiO₂ substrate, we use $\epsilon = 2.5$. The parameter r_0 is the screening length given by $r_0 = 33.875\text{\AA}/\epsilon$ [46]. \mathcal{H}_0 and Y_0 denote the Struve function and Bessel function of the second kind of order zero, respectively, and r represents the electron-hole separation distance.

The annihilation operator $c_{r,o}$ is projected into the eigenstates of Hamiltonian (1) as:

$$c_{r,o} = \sum_{k_x, E=c,v} e^{-ik_x x} \left(\sum_n o_n^E T_n(y) \right) c_{k_x, E}, \quad (7)$$

where o_n^E represents either $a_n^{c,v}$ or $b_n^{c,v}$ components. The Bethe-Salpeter (BS) method [47, 48] given in equation (8) is utilized to derive the exciton dispersion E_Q as a function of the center of mass momentum \mathbf{Q} along the nanoribbon:

$$\iint_{-\frac{L_y}{2}}^{\frac{L_y}{2}} dy dy' \sum_{k_x'} \kappa_{vv'}^{cc'}(y, y', k_x, k_x', Q) \psi_{k_x', Q}^{c', v'} = E_Q \psi_{k_x, Q}^{c, v}. \quad (8)$$

In equation (8) the interaction Kernel is given by:

$$\begin{aligned} \kappa_{vv'}^{cc'}(y, y', k_x, k_x', Q) = \\ (E_{Q+k}^c - E_k^v) \delta_{k_x k_x'} \delta_{cc'} \delta_{vv'} - (\mathcal{D} - \mathcal{X})_{vv'}^{cc'}(y, y', k_x, k_x', Q). \end{aligned} \quad (9)$$

Here, $E_k^{c(v)}$ denotes the quasiparticle energy, represented in Fig. 1(a).

The direct and exchange terms, denoted by \mathcal{D} and \mathcal{X} , respectively, are given by:

$$\mathcal{D}_{vv'}^{cc'}(y, y', k_x, k_x', Q) = V(y-y', k_x-k_x') W_{k_x, k_x'+Q, k_x+Q, k_x'}^{v, c', c, v'}, \quad (10)$$

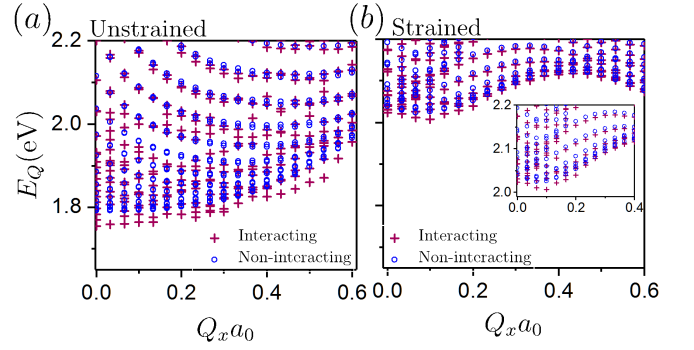


FIG. 3. Exciton energy as a function of center-of-mass momentum Q_x (scaled by a_0), resulting from transitions between the valence band (VB) and conduction band (CB): (a) in the absence of strain and (b) in the presence of strain. The magenta plus symbols represent interacting exciton states, while the blue open circles represent non-interacting exciton states. $N = 20$ is used in the calculations. The inset shows a zoomed-in view of the low-energy exciton states.

and

$$\mathcal{X}_{vv'}^{cc'}(y, y', k_x, k_x', Q) = V(y-y', Q) W_{k_x'+Q, k_x, k_x+Q, k_x'}^{c', v, c, v'}, \quad (11)$$

where $V(y-y', k_x) = \int_0^\infty dx e^{ik_x x} V(y-y', x)$ is the Fourier transform of the Keldysh potential along the nanoribbon's length. The projection of the Keldysh potential into the electronic structure of the twisted nanoribbon is implemented by the functions $W_{q_i}^{E_i}$, which accounts for transitions between valence (v, v') and conduction (c, c') bands and is given by:

$$\begin{aligned} W_{q_1, 2, 3, 4}^{E_1, 2, 3, 4}(y, y') = \\ \sum_{o, o'=a}^b [(\sum_{n_1} O_{n_1, q_1}^* T_{n_1}^*(y)) (\sum_{n_4} O_{n_4, q_4} T_{n_4}(y))]_{E_1 E_4} \\ [(\sum_{n_2} O_{n_2, q_2}^* T_{n_2}^*(y')) (\sum_{n_3} O_{n_3, q_3} T_{n_3}(y'))]_{E_2 E_3}. \end{aligned} \quad (12)$$

Here, E_i and q_i ($i = 1, 2, 3, 4$) represent the energy levels and quantum numbers of the four fermionic operators in, respectively. The functions $O_{n,q}$ and $T_n(y)$ are related to the spinor components and the trigonal basis of the wave functions in the transverse direction.

The exciton dispersion derived using the BS equation (Eq. 8) is presented in Fig. 3. As discussed in the previous section, strain causes an offset between the conduction band minimum and valence band maximum in momentum space. Fig. 3(a) illustrates the bulk excitons in the unstrained case ($\eta = 0$), while Fig. 3(b) corresponds to optical transitions between valence and conduction bands under increasing strain. When strain is applied [Fig. 3(b)], the minimum of the exciton dispersion shifts to a finite momentum $Q_x = q_0$. This strain-induced shift of the exciton dispersion minimum results from the combined effect of strain-induced pseudogauge

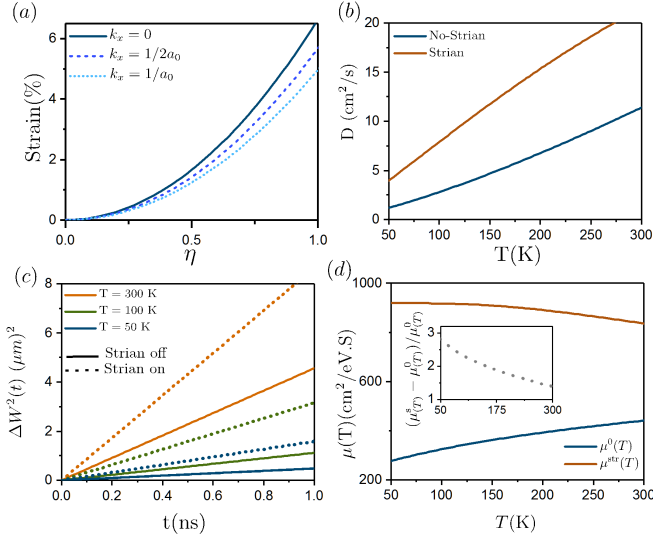


FIG. 4. (a): The strain-induced lattice deformation versus η . The strain parameter $\eta = 1$ corresponds to a $\sim 6\%$ strain, which is considered a safe strain value for the system without risking structural failure. (b): Temperature dependence of exciton diffusion coefficients under strained and unstrained conditions. The result shows a significant enhancement in exciton diffusion due to applied strain. (c): Time evolution of squared broadening widths of excitons at different temperatures for strained (dashed lines) and unstrained (solid lines) cases. (d): Temperature dependence of exciton mobility for strained (Orange) and unstrained (Blue) cases. Inset: Relative mobility $(\mu^{\text{str}}(T) - \mu^0(T))/\mu^0(T)$ as a function of temperature, where $\mu^{\text{str}}(T) - \mu^0(T)$ is the mobility difference between strained and unstrained cases.

field[36] and the presence of band inversion in each valley. The interacting exciton states (magenta symbols) exhibit a lower energy than their non-interacting counterparts (blue open circles), highlighting the role of Coulomb interactions in stabilizing excitons and making them more energetically favorable. This energy reduction is evident both in the absence and presence of strain, although strain modifies the overall dispersion characteristics.

As discussed in Appendix B, it is important to note that while the non-topological case exhibits only minor strain-induced effects on the exciton spectrum, the topological case undergoes significant modifications, as demonstrated in this section.

IV. EXCITON TRANSPORT

As shown in the previous sections, strain not only increases the finite-size-induced gap but also shifts the minimum of the exciton dispersion to a finite center-of-mass momentum [Fig.3(b)]. Strain-induced alterations to the exciton band structure also leads to spatially inhomogeneous exciton distributions that can be described by the

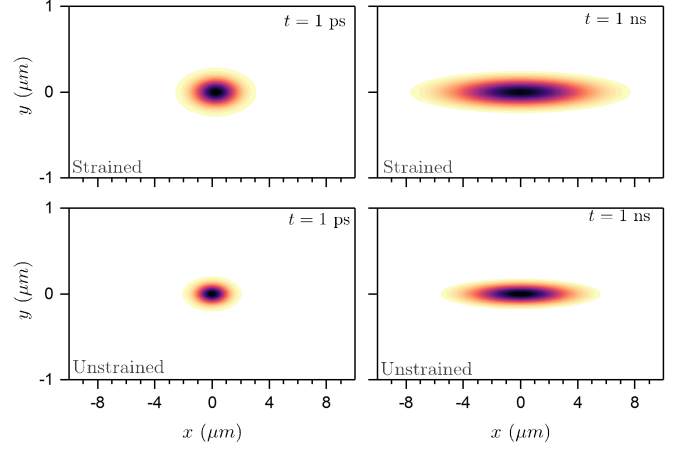


FIG. 5. Spatio-temporal evolution of exciton populations $n(r,t)$ in nanoribbon along x at room temperature $T = 300$ K. The comparison between strained (top) and unstrained (bottom) conditions demonstrates enhanced exciton diffusion induced by strain, measured at times $t = 1$ ps and $t = 1$ ns. The diffusion in the strained (unstrained) case is caused by transitions from ES^* (ES_1) to CB.

exciton continuity equation: [10]

$$\frac{\partial n(r,t)}{\partial t} = \tau \sum_Q \mathbf{v}_Q \cdot \nabla_r (\mathbf{v}_Q \cdot \nabla_r n(r,t) \frac{e^{-E_Q/k_B T}}{\mathcal{Z}}). \quad (13)$$

Here, $n(r,t)$ is the spatiotemporal exciton density, v_Q is the exciton group velocity, τ is the exciton recombination time. The exciton partition function is given by $\mathcal{Z} = \sum_Q e^{-E_Q/k_B T}$, where k_B is the Boltzmann factor and T denotes the temperature.

Using the modified Fick's second law for excitons, i.e., $\partial_t n(r,t) = \mathcal{D} \nabla^2 n(r,t)$ [10, 49], the diffusive motion is described by the diffusion coefficient \mathcal{D} given by:

$$\mathcal{D} = \sum_Q \tau v_Q^2 \frac{e^{-E_Q/k_B T}}{\mathcal{Z}}. \quad (14)$$

Fig. 4(b) illustrates the temperature dependence of the diffusion coefficient enhancement along the nanoribbon after strain is applied. The effect of strain manifests as modifications to the group velocity and exciton energy spectrum E_Q , resulting from strain-induced band structure modulations.

The spatio-temporal evolution of exciton populations is described by the solution of Eq. 13. For an initial delta function distribution $n(r) = n_0 \delta(r)$, the solution is given by a Gaussian function, $n(r,t) = (n_0/\sqrt{\pi \Delta w^2(t)}) e^{-r^2/\Delta w^2(t)}$, where $\Delta w^2(t) = w^2(t) - w_0^2 = 4Dt$ is the squared broadening width. Fig. 4(c) illustrates the time evolution of the squared broadening width $w^2(t)$ of excitons along the nanoribbon. The squared broadening width quantifies the spatial spread of the exciton population over time. The linear relationship between $\Delta w^2(t)$ and t allows for the experimen-

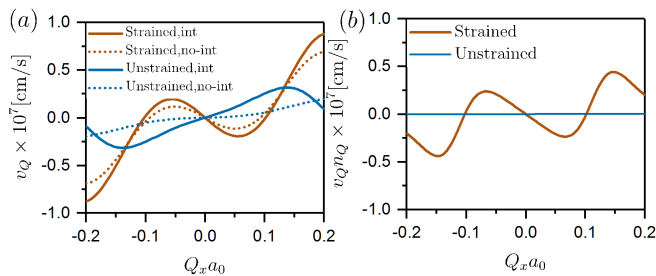


FIG. 6. (a) Group velocity of excitons (v_Q) for strained (brown) and unstrained (blue) systems when interactions between excitons is on (solid line) and off (dotted line) extracted from Fig. 3. Solid lines represent the presence of interactions, while dashed lines indicate their absence. (b) Product of the bosonic distribution function (n_Q) and group velocity (v_Q) as a function of the wavevector ($Q_x a_0$), showing significant oscillations under strain (brown) and negligible values for the unstrained case (blue).

tal determination of the diffusion coefficient by measuring the time-dependent spread of the exciton population [7, 8, 10, 50].

The application of arc-shaped strain to a TMD nanoribbon can also affect carrier mobility. In the unstrained case, excitons typically occupy the lowest energy state at zero momentum ($q_0 = 0$), with mobility primarily determined by diffusion: $\mu_0(T) = D_0(T)/k_B T$ [51], where D_0 is the unstrained diffusion coefficient. However, the shift of the exciton energy minimum to a finite momentum $s q_0$ where $s = \pm 1$, leads to an extra mobility term given by $\mu_d^s(q_0) = v_d^s(q_0)/|\nabla_y E_Q|$, which vanishes after summing over s . Then, the strain-induced mobility would be $\mu(T) = \sum_s D^s(T)/k_B T$, where $D^s(T)$ is the diffusion coefficient in the presence of strain.

Fig. 4(d) presents the temperature-dependent exciton mobility in both strained and unstrained nanoribbons. Our results reveal consistently higher mobility values in the strained case across all temperatures. The inset quantifies this enhancement by showing the relative mobility increase, defined as $(\mu^s(T) - \mu^0(T))/\mu^0(T)$, demonstrating a significant strain-induced mobility enhancement that varies with temperature.

Fig. 5 shows the spatio-temporal evolution of exciton populations $n(r, t)$ along nanoribbon at room temperature, with and without strain. The results demonstrate significant enhancement in exciton diffusion within strained nanoribbons. Due to the finite size gap between the pseudo Landau levels, we modeled the exciton distribution with a time-independent Gaussian profile along the y-axis. The temporal evolution of exciton distribution along x-axis is modeled by the solution of Eq. 13. The enhanced diffusion observed under strain, driven by the strain-induced modifications to the band structure, contrasts with the slower exciton diffusion observed in the unstrained case.

The underlying mechanism for the impact of strain on exciton transport is examined by analyzing the product

of the bosonic distribution function n_Q and the group velocity of excitons $v_Q = (1/\hbar)(\partial_Q E_Q)$. Our results are presented in Fig. 6, which demonstrates that in the unstrained system (blue curves), the product $n_Q v_Q$ remains nearly constant and close to zero across all wavevectors. Under the strain (brown curves), significant variation in $n_Q v_Q$ emerge, suggesting the formation of local exciton currents. These variations exhibit an alternating pattern of positive and negative values of $n_Q v_Q$ around $Q = 0$, leading to the strain-induced modulation of exciton transport. Furthermore, Fig. 6(a) reveals the role of strong electron-hole interactions in shaping exciton dynamics. The solid and dotted lines correspond to cases with and without Coulomb interactions, respectively. In the strained system, interactions enhance the magnitude of the exciton group velocity v_Q , leading to stronger unidirectional exciton diffusion.

V. EXCITON DIPOLE MOMENT

Strong exciton-exciton interactions are crucial for the realization of novel excitonic phases and potential applications. As outlined in the introduction, the shape of the electronic wave functions and their dependence on momentum along the nanoribbon can lead to a larger in-plane dipole moment, which in turn enhances exciton-exciton interactions. This effect can be quantified by estimating the exciton dipole moment, d_{ex} expressed as:

$$d_{ex} = -e \int y \left[|\psi_e(y)|^2 \Big|_{k_e^{\min}} - |\psi_h(y)|^2 \Big|_{k_h^{\max}} \right] dy \quad (15)$$

The terms $|\psi_e(y)|^2$ and $|\psi_h(y)|^2$ represent the probability distributions of the electron and hole, respectively, with their respective wave vectors along the nano-ribbon being at k_e^{\min} and k_h^{\max} . The integral quantifies the net displacement between the electron and hole, determining the magnitude of the dipole moment. Since the exciton dispersion minimum in the presence of strain occurs at a finite center-of-mass momentum, the electron and hole components acquire different momenta. Due to the particular structure of states under a strain-induced gauge field, an electron and hole with different momenta along the nanoribbon correspond to different spatial profiles of their wavefunctions along its width. Such a structure results in a finite in-plane dipole moment. Numerical calculations based on Eq. 15 indicate that strain significantly enhances the dipole moment, increasing it from $d_{ex} \approx 0.5a$ in the unstrained case to $d_{ex} \approx 8a_0$ under strain, where a_0 is the MoS₂ lattice parameter. This enhancement suggests that strain modifies carrier confinement, leading to greater electron-hole separation. We should note that the dependence of exciton dipole moments on their center of mass momentum, is a unique feature of excitons in strained TMDs.

VI. CONCLUSION

We explored the impact of strain on exciton dynamics in TMD nanoribbons. The effects of strain on the low-energy electronic band structure of TMDs manifest as local potentials (which shift the band structure for all momenta) and a pseudo-gauge field (which modifies the dispersion relation). Using the Bethe-Salpeter (BS) formalism, we derived the exciton dispersion in the presence of arc-shaped strain. By increasing the energy gap between states within the valence or conduction bands—relative to the finite-size gap—and shifting the exciton dispersion minimum to a finite center-of-mass momentum, strain extends the exciton lifetime and enhances unidirectional diffusion. Furthermore, excitons in strained TMDs develop a sizable in-plane dipole moment, leading to strong exciton-exciton interactions. Our results demonstrate that strain engineering can be leveraged to design excitonic devices and circuits, where generated excitons diffuse while remaining dark due to their finite center-of-mass momentum and subsequently decay in unstrained regions of the sample.

The formulation of the Bethe-Salpeter equation for excitonic states in a trigonal over-complete basis enables a comprehensive analysis of exciton binding energies and wavefunctions within strain-modulated band structures, where translational symmetry is broken in one direction. Our results on exciton diffusion in strained samples demonstrate how band structure modifications lead to enhanced unidirectional diffusion through increased mobility. Furthermore, our findings reveal that the topological characteristics of each TMD valley play a crucial role in excitonic transport and can potentially be identified through the study of excitonic band structures. Additionally, our method can be applied to different strain patterns to design excitonic circuits.

Given the particular in-plane anisotropic dipole moment of excitons, which also depends on the center-of-mass momentum, strained samples could stabilize novel interacting phases. The study of such interacting excitonic phases will be the focus of future research.

VII. ACKNOWLEDGEMENTS

We acknowledge support from NSF grants DMR 2315063 (PG) and DMR 2130544 (PG and SH). This research was supported in part by grant NSF PHY-2309135 to the Kavli Institute for Theoretical Physics (KITP). We are thankful for fruitful discussions with M. Hafezi, A. Strivitsava, A. Grankin and R. Asgari.

Appendix A: Orthogonal Wave Functions

For a TMD nanoribbon with zigzag edges, the wave function can be expanded using a set of trigonal functions

$T_n(y)$ as

$$\Psi_E(y) = \left(\begin{array}{c} \sum_n a_n^E T_n(y) \\ \sum_n b_n^E T_n(y) \end{array} \right) \quad (\text{A1})$$

where $E = v, c$ denotes the valence and conduction bands, respectively. The index n ranges from 0 to N , with N representing the number of basis functions. It is important to note that these trigonal basis functions do not satisfy the orthogonality condition. Their overlap is given by [20]

$$\langle T_m | T_n \rangle = \frac{L_y^3}{N+1} \left[\frac{2}{3} \delta_{m,n} + \frac{1}{6} (\delta_{m,n+1} + \delta_{m,n-1}) \right] \quad (\text{A2})$$

where $L_y = a_0(N+1)$ is the width of the nanoribbon, and $\delta_{i,j}$ is the Kronecker delta function. However, the wave

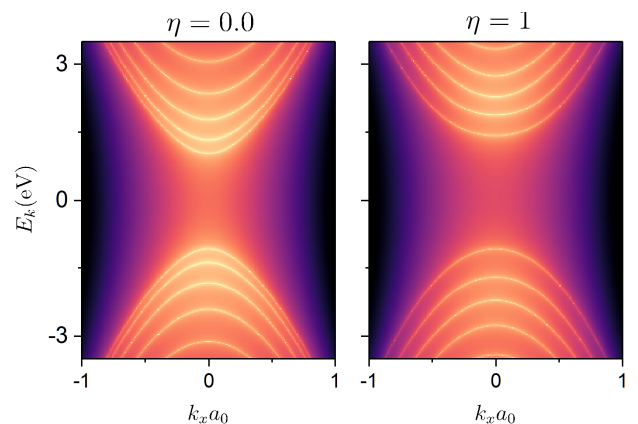


FIG. 7. Non-topological quasiparticle energy dispersion of monolayer MoS₂ nanoribbon around $k_x = 0$, for unstrained case, $\eta = 0$, and arc-shaped strained cases, $\eta \neq 0$. In this figure, the Chern number is set to zero.

function $\Psi_E(y)$ satisfies the following eigenvalue problem:

$$\int dy \Psi_E^*(y) (H - E) \Psi_E(y) = 0 \quad (\text{A3})$$

This leads to:

$$\left(\int dy T_m^*(y) (H - E) T_n(y) \right) \left(\begin{array}{c} \sum_n a_n^E \\ \sum_n b_n^E \end{array} \right) = 0 \quad (\text{A4})$$

where the wave vector $\left(\begin{array}{c} \sum_n a_n^E \\ \sum_n b_n^E \end{array} \right)$ satisfies the orthogonality condition:

$$\sum_{n,m} (a_n^{*E} a_m^{E'} + b_n^{*E} b_m^{E'}) = \delta_{E,E'} \quad (\text{A5})$$

which can be easily verified through numerical calculations.

Appendix B: Non-Topological Case

Fig. 7 demonstrates the non-topological quasiparticle energy dispersion for a monolayer MoS₂ nanoribbon under unstrained ($\eta = 0$) and strained ($\eta = 1$) conditions. In the non-topological regime, the band structure remains mostly unaffected by the strain, showing only minor modifications such as slight flattening and minor energy shifts. Importantly, no edge states emerge in the non-topological case. This is in stark contrast to the topological case, where strain-induced band inversion and edge-state hybridization result in significant changes to the band structure. In the topological case [Fig. 1], the strain introduces edge states that penetrate the bulk and profoundly modify the system's electronic properties, a feature absent in the non-topological scenario. Fig. 8

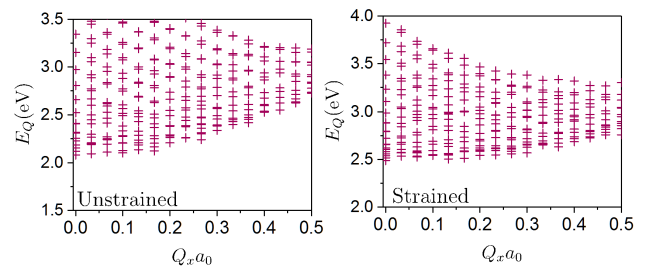


FIG. 8. Exciton energy as a function of center-of-mass momentum Q_x (multiplied by a_0) in the non-topological unstrained and non-topological strained cases. In this figure, the Chern number is set to zero.

compares exciton dispersion for unstrained and strained systems for the non-topological case. According to this figure, the strain has minimal impact on the exciton spectrum, and the energy minimum remains at $Q_x = 0$. In contrast, for the topological case, the strain induces a substantial shift of the exciton energy minimum to finite momentum. This feature of the topological case highlights its potential for strain-engineered unidirectional exciton transport, a behavior not observed in the non-topological system. Furthermore, the topological case exhibits significant excitonic coupling between edge and bulk states, further enhancing its transport properties.

These comparisons underline the profound differences between non-topological and topological regimes in their response to strain, particularly in terms of edge-state behavior and band structure modifications.

-
- [1] L. Lackner, M. Dusel, O. A. Egorov, B. Han, H. Knopf, F. Eilenberger, S. Schroder, K. Watanabe, T. Taniguchi, S. Tongay, *et al.*, Tunable exciton-polaritons emerging from ws2 monolayer excitons in a photonic lattice at room temperature, *Nature communications* **12**, 4933 (2021).
 - [2] T. P. Darlington, C. Carmesin, M. Florian, E. Yanev, O. Ajayi, J. Ardelean, D. A. Rhodes, A. Ghiotto, A. Kravev, K. Watanabe, *et al.*, Imaging strain-localized excitons in nanoscale bubbles of monolayer wse2 at room temperature, *Nature Nanotechnology* **15**, 854 (2020).
 - [3] R. Rosati, R. Schmidt, S. Brem, R. Perea-Causin, I. Niehues, J. Kern, J. A. Preus, R. Schneider, S. Michaelis de Vasconcellos, R. Bratschitsch, *et al.*, Dark exciton anti-funneling in atomically thin semiconductors, *Nature Communications* **12**, 7221 (2021).
 - [4] R. Wallauer, R. Perea-Causin, L. M^unster, S. Zajusch, S. Brem, J. G^udde, K. Tanimura, K.-Q. Lin, R. Huber, E. Malic, *et al.*, Momentum-resolved observation of exciton formation dynamics in monolayer ws2, *Nano letters* **21**, 5867 (2021).
 - [5] Z. Huang, Y. Liu, K. Dini, Q. Tan, Z. Liu, H. Fang, J. Liu, T. Liew, and W. Gao, Robust room temperature valley hall effect of interlayer excitons, *Nano letters* **20**, 1345 (2019).
 - [6] A. Ghazaryan, M. Hafezi, and P. Ghaemi, Anisotropic exciton transport in transition-metal dichalcogenides, *Phys. Rev. B* **97**, 245411 (2018).
 - [7] F. Dirnberger, J. D. Ziegler, P. E. Faria Junior, R. Bushati, T. Taniguchi, K. Watanabe, J. Fabian, D. Bougeard, A. Chernikov, and V. M. Menon, Quasi-1d exciton channels in strain-engineered 2d materials, *Science Advances* **7**, eabj3066 (2021).
 - [8] M. Kulig, J. Zipfel, P. Nagler, S. Blanter, C. Schuller, T. Korn, N. Paradiso, M. M. Glazov, and A. Chernikov, Exciton diffusion and halo effects in monolayer semiconductors, *Phys. Rev. Lett.* **120**, 207401 (2018).
 - [9] A. M. Kumar, D. Yagodkin, R. Rosati, D. J. Bock, C. Schattauer, S. Tobisch, J. Hagel, B. Hofer, J. N. Kirchof, P. Hernandez Lopez, *et al.*, Strain fingerprinting of exciton valley character in 2d semiconductors, *Nature Communications* **15**, 7546 (2024).
 - [10] R. Rosati, S. Brem, R. Perea-Causin, R. Schmidt, I. Niehues, S. M. de Vasconcellos, R. Bratschitsch, and E. Malic, Strain-dependent exciton diffusion in transition metal dichalcogenides, *2D Materials* **8**, 015030 (2020).
 - [11] J. Krustok, R. Kaupmees, R. Jaanisoo, V. Kiisk, I. Sildos, B. Li, and Y. Gong, Local strain-induced band gap fluctuations and exciton localization in aged ws2 monolayers, *AIP Advances* **7**, <https://doi.org/10.1063/1.4985299>

- (2017).
- [12] H. Shi, H. Pan, Y.-W. Zhang, and B. I. Yakobson, Quasi-particle band structures and optical properties of strained monolayer mos2 and ws2, *Phys. Rev. B* **87**, 155304 (2013).
- [13] M. M. Glazov, F. Dirnberger, V. M. Menon, T. Taniguchi, K. Watanabe, D. Bougeard, J. D. Ziegler, and A. Chernikov, Exciton fine structure splitting and linearly polarized emission in strained transition-metal dichalcogenide monolayers, *Phys. Rev. B* **106**, 125303 (2022).
- [14] F. Guinea, M. I. Katsnelson, and A. Geim, Energy gaps and a zero-field quantum hall effect in graphene by strain engineering, *Nature Physics* **6**, 30 (2010).
- [15] N. Levy, S. Burke, K. Meaker, M. Panlasigui, A. Zettl, F. Guinea, A. C. Neto, and M. F. Crommie, Strain-induced pseudo-magnetic fields greater than 300 tesla in graphene nanobubbles, *Science* **329**, 544 (2010).
- [16] P. Nigge, A. Qu, E. Lantagne-Hurtubise, E. Marsell, S. Link, G. Tom, M. Zonno, M. Michiardi, M. Schneider, S. Zhdanovich, *et al.*, Room temperature strain-induced landau levels in graphene on a wafer-scale platform, *Science advances* **5**, eaaw5593 (2019).
- [17] P. Ghaemi, J. Cayssol, D. N. Sheng, and A. Vishwanath, Fractional topological phases and broken time-reversal symmetry in strained graphene, *Phys. Rev. Lett.* **108**, 266801 (2012).
- [18] P. Ghaemi, S. Gopalakrishnan, and S. Ryu, Stability of edge states in strained graphene, *Phys. Rev. B* **87**, 155422 (2013).
- [19] O. L. Berman, R. Y. Kezerashvili, Y. E. Lozovik, and K. G. Ziegler, Strain-induced quantum hall phenomena of excitons in graphene, *Scientific reports* **12**, 2950 (2022).
- [20] H. Rostami, R. Roldan, E. Cappelluti, R. Asgari, and F. Guinea, Theory of strain in single-layer transition metal dichalcogenides, *Phys. Rev. B* **92**, 195402 (2015).
- [21] H. Peelaers and C. G. Van de Walle, Effects of strain on band structure and effective masses in mos2, *Phys. Rev. B* **86**, 241401 (2012).
- [22] F. Shayeganfar, Strain engineering of electronic properties and anomalous valley hall conductivity of transition metal dichalcogenide nanoribbons, *Scientific Reports* **12**, 11285 (2022).
- [23] J. Lee, J. Huang, B. G. Sumpter, and M. Yoon, Strain-engineered optoelectronic properties of 2d transition metal dichalcogenide lateral heterostructures, *2D Materials* **4**, 021016 (2017).
- [24] S. Krishnamurthi and G. Brocks, 1d metallic states at 2d transition metal dichalcogenide semiconductor heterojunctions, *npj 2D Materials and Applications* **5**, 43 (2021).
- [25] D.-H. Choe, H.-J. Sung, and K. J. Chang, Understanding topological phase transition in monolayer transition metal dichalcogenides, *Phys. Rev. B* **93**, 125109 (2016).
- [26] M. M. Ugeda, A. Pulkin, S. Tang, H. Ryu, Q. Wu, Y. Zhang, D. Wong, Z. Pedramrazi, A. Martín-Recio, Y. Chen, *et al.*, Observation of topologically protected states at crystalline phase boundaries in single-layer wse2, *Nature communications* **9**, 3401 (2018).
- [27] H. Rostami and R. Asgari, Intrinsic optical conductivity of modified dirac fermion systems, *Phys. Rev. B* **89**, 115413 (2014).
- [28] P.-Y. Lo, G.-H. Peng, W.-H. Li, Y. Yang, and S.-J. Cheng, Full-zone valley polarization landscape of finite-momentum exciton in transition metal dichalcogenide monolayers, *Phys. Rev. Res.* **3**, 043198 (2021).
- [29] R. E. Prange and S. M. Girvin, eds., *The Quantum Hall Effect* (springer, 1990).
- [30] Z. Sun, A. Ciarrocchi, F. Tagarelli, J. F. Gonzalez Marin, K. Watanabe, T. Taniguchi, and A. Kis, Excitonic transport driven by repulsive dipolar interaction in a van der waals heterostructure, *Nature photonics* **16**, 79 (2022).
- [31] A. Srivastava, M. Sidler, A. V. Allain, D. S. Lembke, A. Kis, and A. Imamoglu, Valley zeeman effect in elementary optical excitations of monolayer wse2, *Nature Physics* **11**, 141 (2015).
- [32] G. Wang, A. Chernikov, M. M. Glazov, T. F. Heinz, X. Marie, T. Amand, and B. Urbaszek, Colloquium: Excitons in atomically thin transition metal dichalcogenides, *Rev. Mod. Phys.* **90**, 021001 (2018).
- [33] R. Y. Kezerashvili, S. M. Tsiklauri, and A. Spiridonova, Controllable trions in buckled two-dimensional materials, *Phys. Rev. B* **110**, 035425 (2024).
- [34] A. Chernikov, T. C. Berkelbach, H. M. Hill, A. Rigosi, Y. Li, B. Aslan, D. R. Reichman, M. S. Hybertsen, and T. F. Heinz, Exciton binding energy and nonhydrogenic rydberg series in monolayer ws2, *Phys. Rev. Lett.* **113**, 076802 (2014).
- [35] E. Cappelluti, R. Roldán, J. A. Silva-Guillén, P. Ordejón, and F. Guinea, Tight-binding model and direct-gap/indirect-gap transition in single-layer and multilayer mos2, *Phys. Rev. B* **88**, 075409 (2013).
- [36] F. de Juan, J. L. Manes, and M. A. H. Vozmediano, Gauge fields from strain in graphene, *Phys. Rev. B* **87**, 165131 (2013).
- [37] M. A. Cazalilla, H. Ochoa, and F. Guinea, Quantum spin hall effect in two-dimensional crystals of transition-metal dichalcogenides, *Phys. Rev. Lett.* **113**, 077201 (2014).
- [38] S. Bertolazzi, J. Brivio, and A. Kis, Stretching and breaking of ultrathin mos2, *ACS nano* **5**, 9703 (2011).
- [39] Z. Li, Y. Lv, L. Ren, J. Li, L. Kong, Y. Zeng, Q. Tao, R. Wu, H. Ma, B. Zhao, *et al.*, Efficient strain modulation of 2d materials via polymer encapsulation, *Nature communications* **11**, 1151 (2020).
- [40] M. Gibertini and N. Marzari, Emergence of one-dimensional wires of free carriers in transition-metal-dichalcogenide nanostructures, *Nano letters* **15**, 6229 (2015).
- [41] M. Vozmediano, M. Katsnelson, and F. Guinea, Gauge fields in graphene, *Physics Reports* **496**, 109 (2010).
- [42] V. M. Pereira, A. H. Castro Neto, and N. M. R. Peres, Tight-binding approach to uniaxial strain in graphene, *Phys. Rev. B* **80**, 045401 (2009).
- [43] Y. C. Cheng, Z. Y. Zhu, W. B. Mi, Z. B. Guo, and U. Schwingenschlogl, Prediction of two-dimensional diluted magnetic semiconductors: Doped monolayer mos2 systems, *Phys. Rev. B* **87**, 100401 (2013).
- [44] L. V. Keldysh, Coulomb interaction in thin semiconductor and semimetal films, *JETP Lett.* **29**, 658 (1979).
- [45] P. Cudazzo, I. V. Tokatly, and A. Rubio, Dielectric screening in two-dimensional insulators: Implications for excitonic and impurity states in graphene, *Phys. Rev. B* **84**, 085406 (2011).
- [46] C. Zhang, H. Wang, W. Chan, C. Manolatu, and F. Rana, Absorption of light by excitons and trions in monolayers of metal dichalcogenide mos2: Experiments and theory, *Phys. Rev. B* **89**, 205436 (2014).
- [47] E. E. Salpeter and H. A. Bethe, A relativistic equation

- for bound-state problems, *Phys. Rev.* **84**, 1232 (1951).
- [48] R. Asgari and D. Culcer, Unidirectional valley-contrasting photocurrent in strained transition metal dichalcogenide monolayers, *Phys. Rev. B* **105**, 195418 (2022).
- [49] J. J. Thompson, S. Brem, M. Verjans, R. Schmidt, S. M. de Vasconcellos, R. Bratschitsch, and E. Malic, Anisotropic exciton diffusion in atomically-thin semiconductors, *2D Materials* **9**, 025008 (2022).
- [50] J. He, D. He, Y. Wang, Q. Cui, F. Ceballos, and H. Zhao, Spatiotemporal dynamics of excitons in monolayer and bulk ws₂, *Nanoscale* **7**, 9526 (2015).
- [51] R. P. Feynman, R. B. Leighton, and M. Sands, *The Feynman lectures on physics, Vol. I: The new millennium edition: mainly mechanics, radiation, and heat*, Vol. 1 (Basic books, 2015).